Universiteit Antwerpen

This item is the archived peer-reviewed author-version of:

Structural intensity assessment on shells via a finite element approximation

uantwerpen.be

Structural intensity assessment on shells via a finite element approximation

Felipe Pires,[1, a)] Stéphane Avril,[2] Steve Vanlanduit,[3, b] and Joris Dirckx[1]

[1]*Department of Physics, University of Antwerp, Groenenborgerlaan 171,*

Antwerp 2020, Belgium

[2]*Mines Saint-Étienne, Université Lyon, INSERM, U 1059 Sainbiose, Centre CIS,*

F, Saint-Étienne 42023, France

[3]*Department of Electromechanical Engineering, University of Antwerp,*

Groenenborgerlaan 171, Antwerp 2020, Belgium

(Dated: 31 January 2019)

The structural intensity on plates or shells can provide insights on how the vibrational energy is transmitted throughout a sample. Its assessment via experimental deflections are widely documented in the case of plates, which just requires the computation of spatial derivatives of out-of-plane displacements or velocities and a knowledge of the sample's material properties. However, if the structural intensity is to be assessed on arbitrary shells, a more elaborate data processing is required. The in-plane displacements become relevant terms and the spatial derivatives along a predefined local coordinate system need to be computed. Here, a method from which experimental data is interpolated on a finite element mesh is proposed. Firstly, the global displacements and shape of a sample's outer-surface are measured. These data are then projected on a quadratic mesh, where the Kirchhoff plate theory is invoked for the individual elements. The data differentiation is computed via quadratic shape functions, from which the strains and structural intensity are estimated. Through the obtained vibrational energy results on the basis of measured displacement and shape data and by validating the method via a numerical simulation, the proposed work has shown to be a reliable tool to assess energy transmission on irregular shells.

[a] felipe.pires@uantwerpen.be; Also at: Department of Mechanical Engineering, Vrije Universiteit Brussel, Pleinlaan 2, Brussels 1050, Belgium

[b] Also at: Department of Mechanical Engineering, Vrije Universiteit Brussel, Pleinlaan 2, Brussels 1050, Belgium

I. INTRODUCTION

The structural intensity (SI) analysis describes the magnitude and direction of vibrational energy being transported by elastic waves in a structure. Such tool was widely used to analyze dominant transmission paths, energy dissipation and source localization in both experimental and numerical studies.

When experimental data of plate-like structures are analyzed, it is convenient to invoke the Kirchhoff-Love postulates (Miguel and Feit, 1986), so the SI can be assessed in terms of the out-of-plane and full-field displacements or velocities and a priori knowledge of the sample's material properties. The quality of the computed energy transmission strongly depends on the signal-to-noise ratio of the experimental deflections, on the amount of measurement points and the employed differentiation technique to estimate the strains and generalized forces.

All these aspects have been improved since the pioneering works regarding the SI assessments via the use of accelerometers during the 70's (Noiseux, 1970; Pavić, 1976). Later on, non-contact measurement techniques permitted the deflections' assessment on denser grids. Examples of reported methods to analyze the vibrational energy are the laser Doppler vibrometry (Arruda and Mas, 1998; Morikawa *et al.*, 1996; Pascal *et al.*, 2002, 2006; Roozen *et al.*, 2015; Schmidt, 2009; Vuye, 2011; Zhang and Mann III, 1996), acoustic-holography (Pascal *et al.*, 1990; Saijyou, 2007), electronic speckle interferometry (Eck and Walsh, 2012), holographic interferometry (Pascal *et al.*, 1996) and digital stroboscopic holography (Pires *et al.*, 2018).

The differentiation of the experimental data has been performed mainly by the finite difference method (Arruda and Mas, 1998; Schmidt, 2009) or by processing and filtering the data in its corresponding wavenumber domain (Arruda, 1992; Lopes *et al.*, 2006; Morikawa *et al.*, 1996; Pascal *et al.*, 1996, 2002, 2006). Such approaches to assess the required spatial derivatives in combination with the described measuring techniques provided meaningful insights in the field, which includes the analysis of plates with peculiar features, such as plates with ribs or joints (Pascal *et al.*, 2006; Semperlotti and Conlon, 2010; Zhang and Mann III, 1996), with cracks (Schmidt, 2009) and with orthotropic material properties (Lamberti and Semperlotti, 2013).

Apart from the SI assessment via experimental data, the use of numerical simulations has also proven to be a useful tool. This approach was not just used to analyze the energy transmission on plates but also on general structures with irregular shapes. The geometries of interest are mainly developed as finite element (FE) models by using solid (Hambric and Szwerc, 1999; Shepherd *et al.*, 2012; Xu *et al.*, 2004a) or shell elements (Gavrić and Pavić, 1993; Hambric, 1990; Lee *et al.*, 2006; Li and Lai, 2000; Liu *et al.*, 2005; Petrone *et al.*, 2016; Xu *et al.*, 2004b). A variety of works were reported in literature, such as the SI study on cracks present in ships or off-shore platforms (Cho *et al.*, 2010; Tian *et al.*, 2017), of locally resonant metamaterials (Al Ba'ba'a *et al.*, 2018; Al Ba'ba'a and Nouh, 2017) and of stiffened or ribbed plates (Cho *et al.*, 2017; Schaal *et al.*, 2016; Xu *et al.*, 2005). Other numerical examples have been also developed to assess the SI on plates containing geometrical or constitutive heterogeneities, such as the case of stepped thickness plates (Cho *et al.*, 2016)

59 and samples with orthotropic material properties (Lamberti and Semperlotti, 2013; Petrone

60 *et al.*, 2016; Tran *et al.*, 2007; Xu *et al.*, 2004b).

61   However, in spite of the advancements in this field, just a few studies regarding the SI on

62 shell-like structures have been developed (Saijyou, 2007; Williams, 1991). Moreover, the SI

63 terms from such samples are conveniently formulated if a set of curvilinear coordinate system

64 is chosen to represent the shell's behavior from its mid-surface (Gavrić and Pavić, 1993). If

65 this approach is chosen, then the spatial derivatives along these very coordinates need to be

66 carried out, so the strains and, in turn, the SI vector components can be retrieved. From

67 these requirements, it can be noted that the definition of these local coordinates depend

68 on the shape of the analyzed sample. Since the in-plane displacement components are no

69 longer negligible (Cho *et al.*, 2010; Gavrić and Pavić, 1993; Romano *et al.*, 1992, 1990; Zhang,

70 1993), full-field experimental data along three orthonormal directions need to be measured.

71 Such demands were not present for the case of plates, whose analysis were just based on the

72 measurement of out-of-plane displacement or velocity fields and whose differentiation could

73 be carried out along a predefined Cartesian coordinate system. Besides, the attempts made

74 so far to analyze the SI on the basis of curvilinear coordinates were restricted to analytical

75 ones, such as the cylindrical or the spherical coordinates (Romano *et al.*, 1990; Saijyou, 2007;

76 Williams, 1991; Zhang, 1993).

77   Apart from these limitations, the standard non-contact measurement techniques cited

78 above are just able to extract data from a sample's outer-surface. Since the displacements

79 may vary with respect to a shell's thickness, extra steps and proper assumptions need to

be taken into account, so the information at the mid-surface can be estimated from the provided data at the sample's outer-surface.

It is the aim of this paper to present a method that tackles the mentioned issues regarding the SI assessment on irregular shells by projecting the experimental data to a FE mesh (Avril *et al.*, 2009; Feng and Rowlands, 1991). The chosen non-contact measurement technique was the Digital Image Correlation (DIC) (Schreier *et al.*, 2009), since it computes both data of interest for this application, i.e., the spatial coordinates describing the shape of the sample's outer-surface and associated displacement data in all three orthonormal directions.

By invoking proper assumptions and approximations, the projected displacements are represented on the basis of a local coordinate system, so all necessary differentiations are computed by choosing proper FE shape functions. The processed data from the outer-surface were then used as input to identify the fields on the mid-surface and the SI was assessed.

All computed SI results showed energy transmission paths that were expected from the analyzed sample. The assessed vector fields of vibrational energy strongly converged to a region on the sample where a viscous damper was installed. Additionally, the accuracy of the data processing proposed in this paper was also tested with the results of a FE shell model. The SI outputs that were acquired via the proposed method and the one provided by the numerical simulation showed similar energy transmission patterns both in magnitude and direction. Due to these findings and by validating this work via a simulation, it is suggested that the current method can handle the major difficulties regarding the SI assessment on arbitrary shells.

II.   THEORY

A.   Structural intensity

It is the aim of this work to assess and visualize the energy paths taking place on ir-

regular shells. This data is defined as the product of the vibration particle velocity and

stress tensor (Morse and Feshbach, 1946; Zhang, 1993), which are quantities that are not

directly measurable on general structures. However, these 2 terms can be related to the

displacements, rotations and generalized forces by making assumptions. By invoking the

Kirchoff-Love postulates (Miguel and Feit, 1986), the time-averaged and active SI per unit

length $[\mathrm{W\,m^{-1}}]$ of a shell under harmonic motion is

$$\mathbf{I} = \mathbf{I}_Q + \mathbf{I}_M + \mathbf{I}_N, \tag{1}$$

where

$$\mathbf{I}_Q = -(\pi f) \begin{Bmatrix} \mathfrak{Im}\{Q_1 u_3^*\} \\ \mathfrak{Im}\{Q_2 u_3^*\} \\ 0 \end{Bmatrix}, \tag{2}$$

$$\mathbf{I}_M = -(\pi f) \begin{Bmatrix} \mathfrak{Im}\{M_{11} a_1^* + M_{12} a_2^*\} \\ \mathfrak{Im}\{M_{21} a_1^* + M_{22} a_2^*\} \\ 0 \end{Bmatrix}, \tag{3}$$

112

$$\mathbf{I}_N = -(\pi f) \left\{ \begin{array}{c} \mathfrak{Im}\{N_{11}u_1^* + N_{12}u_2^*\} \\\\ \mathfrak{Im}\{N_{21}u_1^* + N_{22}u_2^*\} \\\\ 0 \end{array} \right\}. \tag{4}$$

113   Here, f is the frequency at which the structure vibrates, the superscript "$*$" is the complex

114 conjugate symbol and "$\mathfrak{Im}\{\}$" indicates that only the imaginary part of the referred term

115 should be taken into account. The 1$^{\text{st}}$ and 2$^{\text{nd}}$ rows of the vectors $\mathbf{I}_Q$, $\mathbf{I}_M$ and $\mathbf{I}_N$ [Eqs. (2-4)]

116 point at directions that are always tangent to the surface of the analyzed shell, while the

117 3$^{\text{rd}}$ row indicates the normal direction of the surface.

118   Besides, the subscripts "1" and "2" in these equations indicate the directions of the

119 2 tangent coordinates and the subscript "3" indicates the perpendicular one. The defined

120 triad ("1" to "3") correspond to an orthogonal and local coordinate system, which is defined

121 here as $(\mathbf{e}_1, \mathbf{e}_2, \mathbf{e}_3)$. Hence, the unit vectors $\mathbf{e}_1$ and $\mathbf{e}_2$ are always tangent to the shell's surface

122 and the vector $\mathbf{e}_3$ is aligned with the through-thickness coordinate.

123   The terms related to u are the scalar components of the displacements on the mid-surface;

124 and a refers to the rotations about the normals to that very surface. The parameters

125 indicated with the letters Q, N and M are referenced here as the generalized forces taking

126 place on the shell and are the scalar components of the shear force $\mathbf{Q}$, the membrane force

127 $\mathbf{N}$ and the bending moment $\mathbf{M}$, respectively. The development of the equations that relate

128 the generalized forces with displacements or rotations can acquire convenient forms if proper

129 assumptions are used. The next section (Section II B) presents these simplifications, from

130 which $\mathbf{Q}$, $\mathbf{M}$ and $\mathbf{N}$ are derived.

B. Kirchhoff-Love plate model

As it is evident from the experiment described in Section III, the only recorded informa-

tion from the sample are its shape and displacement fields on its outer-surface. The energy

transmission shown in Eqs. (1-4), on the other hand, are defined on a shell's mid-surface.

The relation between the data described in both surfaces depends on the assumtions de-

scribing the analyzed sample. To this end, it is assumed that the shell under study can be

represented as an assembly of elements whose mid-surfaces are planar and whose behavior

can be predicted by the Kirchhoff plate theory.

Since the individual elements are considered to be flat, their curvatures are set to zero

and the second and third fundamental forms vanish from the equations relating the displace-

ments and rotations with the strains (Chapelle and Bathe, 2010). Moreover, the Kirchhoff

plate theory permits the rotation to be estimated directly from the outer-surface, since this

parameter is assumed to be independent from the through-thickness coordinate. The as-

sumed theory also permits the relations between the data from the outer-surface and energy

transmission from the mid-surface to be conveniently developed, since the displacements

and strains vary linearly with respect to the shell's normal direction. Due to all these sim-

plifications, the generalized forces acquire relatively simpler forms and can be estimated on

the basis of data recorded from a sample's outer-surface.

1.   *Kinematics of shells*

150   The equations supporting the proposed data processing of this work are entirely based on

151   the Kirchhoff-Love plate model for shells; which, in turn, obeys the Kirchhoff-Love postu-

152   lates (Miguel and Feit, 1986). By recalling the assumption that the shell's normal direction

153   undergo no change in length during deformation (Kraus, 1967), one can state that the

154   displacement has a linear distribution in its normal direction (Bischoff and Ramm, 1997;

155   Büchter *et al.*, 1994) and the following relation holds:

$$\mathbf{u}^{h/2} = \mathbf{u} + \frac{h}{2}\mathbf{a}, \tag{5}$$

156   where $\mathbf{u}$ is the displacement vector field at the mid-surface of the shell, $\mathbf{a}$ is the rotation

157   about the normal to that very surface, h is the thickness value of the shell and the $\mathbf{u}^{h/2}$ is

158   the displacement on the outer-surface.

159   As it was the case for Eq. (1), the scalar components of $\mathbf{u}^{h/2}$, $\mathbf{u}$ and $\mathbf{a}$ also correspond to

160   the orthogonal coordinate system $(\mathbf{e}_1, \mathbf{e}_2, \mathbf{e}_3)$. Hence,

$$\mathbf{u}^{h/2} = \left\{ \begin{array}{c} u_1^{h/2} \\ u_2^{h/2} \\ u_3^{h/2} \end{array} \right\}, \quad \mathbf{u} = \left\{ \begin{array}{c} u_1 \\ u_2 \\ u_3 \end{array} \right\}, \quad \mathbf{a} = \left\{ \begin{array}{c} a_1 \\ a_2 \\ 0 \end{array} \right\}, \tag{6}$$

161   where the in-plane directions of the displacements and rotations are indicated by the sub-

162   script "1" and "2"; and the subscript "3" indicates the scalar field along the out-of-plane

163   direction.

164   By recalling the assumptions of the Kirchhoff-Love plate model once again, one can relate

165   the linearlized Green-Lagrange strain on the outer-surface $\boldsymbol{\varepsilon}^{h/2}$ as a function of the membrane

166 and bending strains (Chapelle and Bathe, 2010), i.e.,

$$\boldsymbol{\varepsilon}^{h/2} = \boldsymbol{\gamma} + \frac{h}{2}\boldsymbol{\chi}, \tag{7}$$

167 where $\boldsymbol{\gamma}$ is the membrane strain and $\boldsymbol{\chi}$ is the bending strain linearly varying over the shell's

168 thickness. The scalar components of the vectors in Eq. (7) are

$$\boldsymbol{\varepsilon}^{h/2} = \left\{ \begin{array}{c} \varepsilon_{11}^{h/2} \\ \varepsilon_{22}^{h/2} \\ \varepsilon_{12}^{h/2} \end{array} \right\}, \quad \boldsymbol{\gamma} = \left\{ \begin{array}{c} \gamma_{11} \\ \gamma_{22} \\ \gamma_{12} \end{array} \right\}, \quad \boldsymbol{\chi} = \left\{ \begin{array}{c} \chi_{11} \\ \chi_{22} \\ \chi_{12} \end{array} \right\}, \tag{8}$$

169 By knowing that the elements describing the assembly are planar, the strains $\boldsymbol{\varepsilon}^{h/2}$ and $\boldsymbol{\chi}$

170 can be interpreted as functions of the displacement and rotation being differentiated along

171 the local coordinates $\mathbf{e}_1$ and $\mathbf{e}_2$. Hence,

$$\varepsilon_{ij}^{h/2} = \frac{1}{2}(u_{i,j}^{h/2} + u_{j,i}^{h/2}), \quad \text{for} \quad i,j = \{1,2\}, \tag{9}$$

172 and

$$\chi_{ij} = \frac{1}{2}(a_{i,j} + a_{j,i}), \quad \text{for} \quad i,j = \{1,2\}, \tag{10}$$

173 where the subscripts ",i" or ",j" indicate that the fields are differentiated along the direc-

174 tions "i" or "j", respectively.

175 **2. Generalized forces**

176 Since the strains' formulations are available, the non-negligible stress components can

177 be defined as functions of the strain varying linearly with respect to the through-thickness

178 coordinate ζ and the shell's material properties. Therefore, it follows that

$$\boldsymbol{\sigma}^\zeta = \boldsymbol{\Omega}\boldsymbol{\varepsilon}^\zeta, \tag{11}$$

179 where $\boldsymbol{\Omega}$ is the stiffness matrix, $\boldsymbol{\sigma}^\zeta$ is the stress as a function of the through-thickness

180 coordinate ζ and $\boldsymbol{\varepsilon}^\zeta$ is the Green-Lagrange strain as a function of ζ. These parameters are

181 defined as

$$\boldsymbol{\Omega} = \frac{E}{1-\nu^2} \begin{bmatrix} 1 & \nu & 0 \\ \nu & 1 & 0 \\ 0 & 0 & 1-\nu \end{bmatrix}, \tag{12}$$

182

$$\boldsymbol{\sigma}^\zeta = \begin{Bmatrix} \sigma_{11}^\zeta \\ \sigma_{22}^\zeta \\ \sigma_{12}^\zeta \end{Bmatrix}, \quad \boldsymbol{\varepsilon}^\zeta = \begin{Bmatrix} \varepsilon_{11}^\zeta \\ \varepsilon_{22}^\zeta \\ \varepsilon_{12}^\zeta \end{Bmatrix}, \tag{13}$$

183   By integrating Eq. (11) with respect to the through-thickness coordinate ζ, the general-

184 ized forces related to the membrane strain $\boldsymbol{\gamma}$ and the bending strain $\boldsymbol{\chi}$ can be computed:

185

$$\mathbf{N} = h\boldsymbol{\Omega}\boldsymbol{\gamma}, \tag{14}$$

186

$$\mathbf{M} = \frac{h^3}{12}\boldsymbol{\Omega}\boldsymbol{\chi}, \tag{15}$$

being the components of the membrane force $\mathbf{N}$ and bending moment $\mathbf{M}$ defined as

$$\mathbf{N} = \left\{ \begin{array}{c} N_{11} \\ N_{22} \\ N_{12} \end{array} \right\}, \quad \mathbf{M} = \left\{ \begin{array}{c} M_{11} \\ M_{22} \\ M_{12} \end{array} \right\}, \tag{16}$$

and where

$$M_{21} = M_{12}, \quad N_{21} = N_{12}, \tag{17}$$

from (Novozhilov, 1959) and by considering the current case of a Kirchhoff-Love plate model (Chapelle and Bathe, 2010).

The internal forces related to the shear force $\mathbf{Q}$ are assessed by analyzing the equilibrium conditions of a differential element and by taking into account that the shell is being represented by an assembly of plates. Through the equilibrium conditions, the shear force acquires the following form (Ventsel and Krauthammer, 2001):

$$\mathbf{Q} = \left\{ \begin{array}{c} Q_1 \\ Q_2 \end{array} \right\} = \left\{ \begin{array}{c} M_{11,1} + M_{12,2} \\ M_{12,1} + M_{22,2} \end{array} \right\}, \tag{18}$$

It can be noted from Eq. (18) that the shear force is dependent on the spatial derivatives of the bending moment. If the scalar components of Eq. (15) are differentiated, it holds that

$$M_{ii,i} = \frac{h^3}{12} \frac{E}{1-\nu^2} (\chi_{ii,i} + \nu \chi_{jj,i}), \quad \text{for} \ \ i,j = \{1,2\}, \tag{19}$$

$$M_{ij,i} = \frac{h^3}{12} \frac{E}{1+\nu} \chi_{ij,i}, \quad \text{for} \ \ i,j = \{1,2\}. \tag{20}$$

The derivatives of χ_{ij} in Eqs. (19, 20) can be acquired by differentiating the bending strain $\boldsymbol{\chi}$ in Eq. (10):

$$\chi_{ij,i} = \frac{1}{2}(a_{i,ij} + a_{j,ii}), \quad \text{for} \quad i,j = \{1,2\}, \tag{21}$$

where $\chi_{ij,i}$ is a scalar component of $\boldsymbol{\chi}_{,i}$. From the derivations shown in Eqs. (18-21), it is clear that in order to access $\mathbf{Q}$, the 2$^{\text{nd}}$ order derivatives of the rotation (presented throughout this work as $\mathbf{a}_{,ij}$) are required.

3. Assessment of data on the mid-surface

The equations provided so far are given to support the processing from the data available at the outer-surface of a sample, i.e., the terms $\mathbf{u}^{h/2}$ and $\mathbf{a}$ from Eq. (5); and $\boldsymbol{\varepsilon}^{h/2}$ and $\boldsymbol{\chi}$ from Eq. (7). By analyzing the SI scalar components in Eqs. (2-4), it can be noted that the terms related to the displacement on the mid-surface $\mathbf{u}$ would still be missing. Moreover, the membrane force $\mathbf{N}$ can not be directly estimated, since it is formulated as a function of the membrane strain $\boldsymbol{\gamma}$, which is also a parameter from a shell's mid-surface.

The approach used to assess both the displacement $\mathbf{u}$ and the membrane strain $\boldsymbol{\gamma}$ was simply to isolate these very terms from Eqs. (5, 7). By assuming that one has a previous knowledge of all other terms, the displacement and strain on the mid-surface can be recovered from

$$\mathbf{u} = \mathbf{u}^{h/2} - \frac{h}{2}\mathbf{a}, \tag{22}$$

and

$$\boldsymbol{\gamma} = \boldsymbol{\varepsilon}^{h/2} - \frac{h}{2}\boldsymbol{\chi}. \tag{23}$$

216 If the term $\boldsymbol{\chi}_{,i}$ is also at hand, all generalized forces ($\mathbf{N}$, $\mathbf{M}$ and $\mathbf{Q}$) can be assessed from

217 Eqs. (14, 15, 18-20) and it is possible to estimate the SI on the basis of Eqs. (1-4).

218   By adopting the Kirchhoff-love plate model to represent a real sample, one can also

219 state that such an assembly can be treated as a FE mesh, whose local Degrees of Freedom

220 (DoFs) are the displacement $\mathbf{u}$ and rotation $\mathbf{a}$ [Eq. (5)]. By choosing proper shape functions,

221 these DoFs can be differentiated along the directions $\mathbf{e}_1$ and $\mathbf{e}_2$ [Eqs. (9, 10, 21)] and the

222 generalized forces can be assessed.

223   However, as it will be pointed out in Section III, the experimental displacements from

224 the outer-surface that are exported from the developed set-up are defined on a Cartesian

225 coordinate system ($\mathbf{e}_x$, $\mathbf{e}_y$, $\mathbf{e}_z$) (defined throughout this work as $\mathbf{U}_{exp}^{h/2}$). Moreover, the spatial

226 coordinates of the FE mesh's nodes are usually not equal in number or position with the

227 coordinates from which the experimental data $\mathbf{U}_{exp}^{h/2}$ is recorded.

228   Due to these 2 issues, the measurements need to be first projected from the dense ex-

229 perimental point cloud to the nodes of a mesh and then a transformation of coordinate

230 systems needs to take place. Both issues are addressed in detail in Sections II C and II E,

231 respectively.

232 **C. Data projection on a finite element mesh**

233   It can be noted from Section II B 2 that in order to assess $\mathbf{Q}$, $\mathbf{N}$ and $\mathbf{M}$; 1st order

234 derivatives of $\mathbf{u}$ [Eq. (9)] and 2nd order derivatives of $\mathbf{a}$ [Eq. (21)] need to be computed. This

235 work proposes the processing of these spatial derivatives via FE shape functions.

It follows that a generalized vector field $\hat{\boldsymbol{\psi}}$ can be calculated at any position $\mathbf{x}$ within an element by interpolating the information stored at its nodes and predefined shape functions N. Therefore, it holds that

$$\hat{\boldsymbol{\psi}}(\mathbf{x}) = \sum_{b=1}^{c} N_b(\mathbf{x}) \cdot \tilde{\boldsymbol{\psi}}_b, \tag{24}$$

being "c" the total number of nodes present in an FE element, $\tilde{\boldsymbol{\psi}}$ is a generalized DoF stored on the mesh's nodes and the subscript "b" depicts the node numbering of the field $\tilde{\boldsymbol{\psi}}$ and the shape function N.

The approach used to perform the projection of experimental data on a mesh was the global least-squares minimization via FE shape functions (Avril *et al.*, 2009; Avril and Pierron, 2007; Feng and Rowlands, 1991) over the whole sample's measurement domain. The minimization problem is defined as

$$\min \sum_{a=1}^{d} \left| \hat{\boldsymbol{\psi}}(\mathbf{x}_a) - \boldsymbol{\psi}(\mathbf{x}_a) \right|^2, \tag{25}$$

where $\boldsymbol{\psi}$ refers to a generalized experimental data and d is the total number of evaluated points of $\boldsymbol{\psi}$. By substituting $\hat{\boldsymbol{\psi}}$ with the right-handed terms of Eq. (24) and by considering $\boldsymbol{\Phi}$, $\tilde{\Psi}$ and Ψ the assembled matrices of $N(\mathbf{x}_a)$, $\tilde{\boldsymbol{\psi}}(\mathbf{x}_a)$ and $\boldsymbol{\psi}(\mathbf{x}_a)$, respectively; Eq. (25) can be represented in its assembled matrix form as

$$\tilde{\Psi} = \left[\left[\boldsymbol{\Phi}^T \boldsymbol{\Phi} \right]^{-1} \boldsymbol{\Phi}^T \right] \Psi. \tag{26}$$

From here, it becomes evident that the measured full-field data Ψ, their corresponding spatial coordinates $\mathbf{x}_a$ and defined basis functions $N(\mathbf{x}_a)$ are sufficient inputs to solve the minimization problem. At the end of this process, one has access to the assembled data $\tilde{\Psi}$ at the nodal points of a FE mesh.

254   In the current work, the experimental displacements $\mathbf{U}_{exp}^{h/2}$ and related spatial coordinates

255   $\mathbf{x}$ on the outer-surface are the data that will be projected on the mesh. If these 2 terms are

256   available, one has all the necessary inputs of Eq. (26), so the projection procedure can take

257   place on the mesh. By substituting Ψ with $\mathbf{U}_{exp}^{h/2}$ in Eq. (26), it is concluded that

$$\tilde{\mathbf{U}}^{h/2} = \left[\left[\boldsymbol{\Phi}^T \boldsymbol{\Phi} \right]^{-1} \boldsymbol{\Phi}^T \right] \mathbf{U}_{exp}^{h/2}. \tag{27}$$

258   being $\tilde{\mathbf{U}}^{h/2}$ the displacements of the outer-surface and stored on the mesh's nodes.

259   **D.   Assessment of rotations**

260   Since the Kirchhoff plate theory is being imposed on the shell's elements, the rotation

261   at each node can be computed by subtracting the normal directions of the mesh under its

262   deformed configuration with the ones in the reference configuration (Bischoff and Ramm,

263   1997; Murthy and Gallagher, 1986; Wagner and Gruttmann, 1994). Moreover, due to the

264   assumption stating that the normal direction of the mid-surface remains perpendicular to

265   that very surface after deformation, the subtraction's result becomes independent from the

266   local coordinate ζ. Hence, this operation can be done at $\zeta = h/2$, which is the region where

267   the experimental data are extracted from.

268   By assuming that the term $\tilde{\mathbf{U}}^{h/2}$ and the mesh are at hand, the rotation corresponding

269   to the stationary Cartesian coordinate system ($\tilde{\mathbf{A}}$) can be assessed. This is achieved by

270   subtracting the normal directions of the mesh at its deformed state ($\mathbf{n}_{def}$) from its reference

271   state ($\mathbf{e}_3$). The deformed state of the mesh is computed by translating the nodes at the

272   direction provided by the displacements $\tilde{\mathbf{U}}^{h/2}$. The unit vectors $\mathbf{n}_{def}$ are then computed and

17

273 the subtraction can take place. Therefore, it holds that

$$\tilde{\mathbf{A}} = \mathbf{n}_{def} - \mathbf{e}_3. \tag{28}$$

274 By accomplishing this step, each node of the FE mesh should have 6 DoFs that are aligned

275 with $(\mathbf{e}_x, \mathbf{e}_y, \mathbf{e}_z)$: 3 scalar components of $\tilde{\mathbf{U}}^{h/2}$ and other 3 of $\tilde{\mathbf{A}}$.

E. Coordinate system transformation & data differentiation

277 As pointed out in Section II B 3, the computation of Eqs. (2-4) requires that the displace-

278 ment and rotation be aligned with the local triad $(\mathbf{e}_1, \mathbf{e}_2, \mathbf{e}_3)$. With a previous knowledge of

279 these coordinates, the orthonormal basis representing $\tilde{\mathbf{U}}^{h/2}$ and $\tilde{\mathbf{A}}$ are rotated accordingly

280 in each element and their components in the local coordinates are obtained. These terms

281 are denoted here as $\tilde{\mathbf{u}}^{h/2}$ and $\tilde{\mathbf{a}}$ and are also stored on the mesh's nodes.

282 It was stated previously that 2nd order derivatives of $\mathbf{a}$ need to be computed to access

283 the shear forces [Eq. (18-21)]. Therefore, the Kirchhoff-Love plate model requires at least

284 quadratic shape functions, so this higher-order differentiation can be processed.

285 The proposed work makes use of triangular elements to develop the FE mesh, since it

286 is the most popular element for estimating in-plane related variables (Dhatt *et al.*, 1986)

287 and is capable of discretizing arbitrary shells efficiently. By applying quadratic shape func-

288 tions on this assembly, it holds that the FE mesh is build upon a collection of 6-noded

289 triangules (Zienkiewicz *et al.*, 1977), i.e., linear-strain triangular elements (LST).

By defining that each element has 6 nodes and by substituting $\tilde{\boldsymbol{\psi}}$ for either $\tilde{\mathbf{u}}^{h/2}$ or $\tilde{\mathbf{a}}$ in Eq. (24), it holds that

$$\hat{\mathbf{u}}^{h/2}(\mathbf{x}) = \sum_{b=1}^{6} N_b(\mathbf{x}) \cdot \tilde{\mathbf{u}}_b^{h/2}, \quad \hat{\mathbf{a}}(\mathbf{x}) = \sum_{b=1}^{6} N_b(\mathbf{x}) \cdot \tilde{\mathbf{a}}_b, \tag{29}$$

where $\hat{\mathbf{u}}^{h/2}$ and $\hat{\mathbf{a}}$ are the displacement and rotation being evaluated at the position $\mathbf{x}$ inside an element.

For the purpose of this work, it was decided to evaluate the shell's behavior at the barycentric coordinates of the FE mesh's elements. Hence, by defining $\bar{N}$ to be the shape functions being evaluated at these very coordinates and by substituting them into Eq. (29),

$$\mathbf{u}^{h/2} = \sum_{b=1}^{6} \bar{N}_b \cdot \tilde{\mathbf{u}}_b^{h/2}, \quad \mathbf{a} = \sum_{b=1}^{6} \bar{N}_b \cdot \tilde{\mathbf{a}}_b. \tag{30}$$

being $\mathbf{u}^{h/2}$ and $\mathbf{a}$ the terms present in Eq. (5).

As it is the case for the left-handed terms of Eq. (30), their spatial derivatives are also estimated on the barycenter of the elements. It could be seen from Eqs. (9, 21) that 1st order derivatives of $\mathbf{u}^{h/2}$ and 2st order derivatives of $\mathbf{a}$ are required for the SI assessment Eqs. (2-4).

By differentiating the shape functions terms in Eq. (30) to the demanded differentiation orders, it holds that

$$\mathbf{u}_{,i}^{h/2} = \sum_{b=1}^{6} \bar{N}_{b,i} \cdot \tilde{\mathbf{u}}_b^{h/2}, \tag{31}$$

$$\mathbf{a}_{,i} = \sum_{b=1}^{6} \bar{N}_{b,i} \cdot \tilde{\mathbf{a}}_b, \quad \mathbf{a}_{,ij} = \sum_{b=1}^{6} \bar{N}_{b,ij} \cdot \tilde{\mathbf{a}}_b, \tag{32}$$

₃₀₆ where the terms $\mathbf{u}_{,i}^{h/2}$; $\mathbf{a}_{,i}$ and $\mathbf{a}_{,ij}$ are spatial derivatives along the local directions "i" or "j"

₃₀₇ and which are present in Eqs. (9, 10, 21). By making use of the Eqs.(30-32), the strains and

₃₀₈ related derivatives $\boldsymbol{\varepsilon}^{h/2}$, $\boldsymbol{\chi}$ and $\boldsymbol{\chi}_{,i}$ [Eqs. (9, 10, 21)] can be also assessed. From these terms,

₃₀₉ the fields related to the element's mid-surfaces $\mathbf{u}$ and $\boldsymbol{\gamma}$ are estimated via the Eqs. (22, 23)

₃₁₀ and from which all generalized forces [Eqs. (14, 15, 18-20)] and, in turn, the SI [Eqs. (1-4)]

₃₁₁ can be computed.

III. MATERIALS

₃₁₃ The measurement of full-field displacements and subsequent data processing was per-

₃₁₄ formed on a circular membrane made of silicon, whose boundaries were fixed (FIG. 1). Its

₃₁₅ Young's modulus E was estimated to be 8 MPa through a tensile test, its Poisson's coef-

₃₁₆ ficient ν was assumed to be 0,3; and its thickness and diameter were 1 mm and 12 cm,

₃₁₇ respectively.

₃₁₈ The device that disturbed this specimen was a loudspeaker (TOA Corporation, TU-650,

₃₁₉ Tokyo, Japan). The delivered excitation pressure was set to a single frequency, while a

₃₂₀ full-field displacement measurement was being performed. Since it was desired to visualize

₃₂₁ energy paths of the SI on the silicon membrane, a strip of a synthetic viscoelastic urethane

₃₂₂ polymer (Thorlabs, SB12B Sorbothane Sheet, NJ, USA) was fixed from one of its extreme

₃₂₃ sides with the center of the membrane, so the the power being provided by the loudspeaker

₃₂₄ would be absorbed on that region (depicted as "damper" in the cross-section view of FIG. 1).

₃₂₅ The region between the loudspeaker and the membrane was isolated in a chamber to ensure

₃₂₆ that most of the delivered power would be directed to the specimen.

327 Since the final aim of this work is to process displacement and shape data on irregular

328 shells, the manipulation of the membrane's shape was accomplished by moving the other

329 extreme end of the polymer strip. By pulling this material, the membrane would gradually

330 obtain a curved-conical shape in its reference configuration.

331 To avoid the presence of pre-strains in the resting position by excessively pulling the

332 damper, the membrane's boundaries were clamped in such a way that membrane would not

333 be stretched at first, leaving it loose and with "wrinkles". Afterwards, the viscous polymer

334 was attached to the membrane's surface from the chamber's interior.

335 The polymer was then carefully pulled from the its free end and from inside the chamber.

336 The pulling of the damper would stop at the moment where the membrane's "wrinkles"

337 would cease to exist. This qualitative and visual calibration would indicate that the specimen

338 would be on the verge of having residual strains if the damper would be further pulled. At

339 the end of this process, the free end of the polymer was fixed and the curved-conical shape of

340 the membrane would be acquired. Moreover, the outer-surface of the membrane was sprayed

341 on with a black-acrylic ink and a fine speckle pattern was drawn on its surface.

342 The measurement of membrane's spatial coordinates at its resting configuration ($\mathbf{x}$) and

343 densely distributed displacement measurements on that surface were obtained via the DIC

344 technique (Schreier *et al.*, 2009). For this aim, a Q-400 digital 3D image correlation system

345 provided by Dantec/Limess was used. The membrane's dynamic behavior was captured by

346 two high-speed camera's (see FIG. 1) and the images' evaluation was carried out by the

347 Istra4D software provided by the system.

348 The normalization of the displacement and processed data was calculated by using the

349 excitation pressure as references. This parameter was measured by a probe microphone

350 (Brüel & Kjær, Type 4182, Nærum, Denmark), which was installed inside the chamber.

351 The device was fixed near the membrane and the distance between its tip and the specimen

352 was approximately 2 mm.

353 The computation of the shape's spatial coordinates and normalized displacement were

354 carried out under several excitation frequencies. To ensure that the harmonic excitation

355 pressure would be uniform throughout the membrane's surface, it was decided to perform

356 the dynamic analysis on low excitation frequencies only (ranging from 60 Hz up to 170 Hz).

357 As it was already mentioned, second order spatial derivatives of the data need to be

358 computed and the quality of these differentiations are highly dependent on the signal-to-

359 noise ratio of the measured displacement fields. Therefore, it has been decided to filter

360 the displacement fields to ensure that the influence of noise is diminished before the data

361 projection on a mesh. The chosen approach for this work was to apply an in-house Gaussian

362 filter with a standard deviation of 1 on every displacement field. From now on, these

363 filtered global displacement fields are referenced here as the term $\mathbf{U}_{exp}^{h/2}$, which was cited in

364 Section II C and in Eq. (27).

365 After performing the measurements on the circular membrane, the terms $\mathbf{U}_{exp}^{h/2}$ and $\mathbf{x}$ are

366 obtained. These two groups of experimental parameters were then used to assess the SI

367 under different excitation frequencies. The procedure from which the energy transmission

368 paths are computed from $\mathbf{U}_{exp}^{h/2}$ and $\mathbf{x}$ are described in the following section (Section IV).

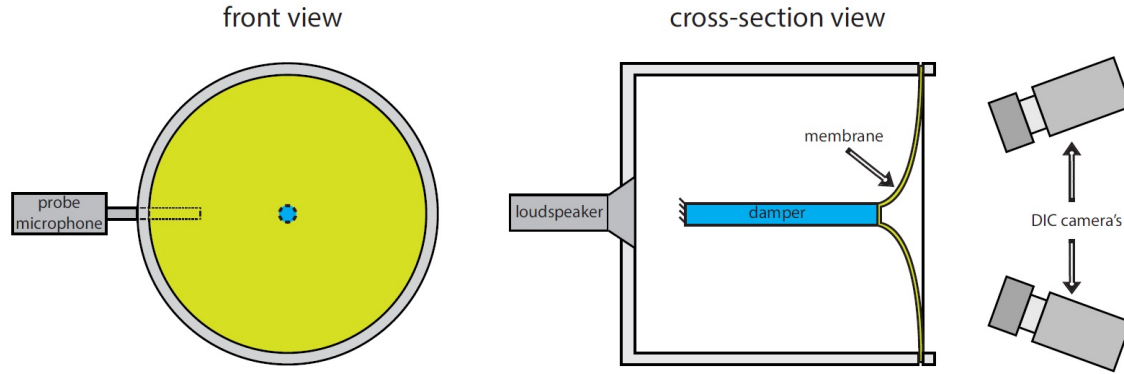FIG. 1. Set-up configuration (color online)

IV.   METHODS

A.   Measurements via the Digital Image Correlation technique

After preparing the set-up described in Section III, the circular membrane was disturbed by the loudspeaker under several excitation frequencies ranging from 60 Hz to 170 Hz. The high-speed camera's captured the membrane's motion and the recorded images were correlated with the support of the Istra4D software.

The spatial coordinates of the membrane in its resting configuration $\mathbf{x}$ could then be generated and full-field displacements $\mathbf{U}_{exp}^{h/2}$ of that sample were computed in several frequencies. At the end of this step, both groups of data were exported for further processing.

B.   Mesh generation & definition of the local coordinate system

By possessing the data $\mathbf{x}$, it is feasible to create a mesh whose shape would overlap the original spatial coordinates of the membrane. As it was pointed out in Section II E,

381 the current application requires at least quadratic elements to be the constituents of the

382 developed mesh and it was decided to use triangular elements for the whole domain.

383 A considerable number of these experimental points need to be projected on each element

384 of the mesh, so the interpolated coefficients (located at the nodes) could have trustworthy

385 results. Based on this concept, the elements should be big enough to encompass a significant

386 amount of data points. On the other hand, the mesh should be fine enough to ensure

387 that the geometry's shape and curvatures are preserved. Therefore, it can be noted that

388 the generation of the elements' size heavily depends on how many measuring points were

389 recorded with the DIC set-up.

390 After creating a mesh based on the density of experimental data, it was defined that the

391 local coordinates $\mathbf{e}_1$ and $\mathbf{e}_2$ would be the principal curvature directions of the generated shell.

392 These vector fields were computed via a multi-scale curvature estimation method (Panozzo

393 *et al.*, 2010) and with the support of an open-source library for geometry processing named

394 as LIBIGL (Jacobson *et al.*, 2017). The computation of the third direction $\mathbf{e}_3$ was obtained

395 by computing the normal direction of each element. At the end of this procedure, the local

396 basis of unit vectors ($\mathbf{e}_1$, $\mathbf{e}_2$, $\mathbf{e}_3$) was defined.

397 **C. Assessment of the global displacements & rotations**

398 Not just the terms $\mathbf{U}_{exp}^{h/2}$ and $\mathbf{x}$ should be available at this point, but the spatial coordinates

399 of the nodes of the mesh and the quadratic shape functions are also known. With all these

400 terms at hand, one has all inputs of Eq. (27) and the global degrees of freedom related to the

401 displacement $\tilde{\mathbf{U}}^{h/2}$ can be computed. Afterwards, the normal direction of the mesh under

its deformed state $\mathbf{n}_{def}$ was estimated with the purpose of extracting the missing global rotation $\tilde{\mathbf{A}}$ through Eq. (28).

After storing the fields $\tilde{\mathbf{U}}^{h/2}$ and $\tilde{\mathbf{A}}$ at the nodes of the mesh and by having a priori knowledge of the local coordinates $(\mathbf{e}_1, \mathbf{e}_2, \mathbf{e}_3)$ of the shell, a change of basis vectors can be computed for each element as described in Section II E. By performing the change of basis of unit vectors, the fields $\tilde{\mathbf{u}}^{h/2}$ and $\tilde{\mathbf{a}}$ are made available.

D. Data differentiation, mid-surface terms, generalized forces & structural intensity

The terms $\tilde{\mathbf{u}}^{h/2}$ and $\tilde{\mathbf{a}}$ in combination with the quadratic shape functions are then used to compute these very fields and the required spatial derivatives at the elements' barycentric coordinates [Eqs. (30-32)]. The terms $\mathbf{u}_{,i}^{h/2}$ and $\mathbf{a}_{,i}$ are then used as inputs in Eqs. (9, 10) to assess the strains $\boldsymbol{\varepsilon}^{h/2}$ and $\boldsymbol{\chi}$, while the term $\mathbf{a}_{,ij}$ is used to compute $\boldsymbol{\chi}_{,i}$ [Eq. (21)]. At the end of this process, the terms $\boldsymbol{\varepsilon}^{h/2}$, $\boldsymbol{\chi}$ and $\boldsymbol{\chi}_{,i}$ are available.

All terms at the right-hand side of the Eqs. (22, 23) should be available at this point and the displacement $\mathbf{u}$ and strains $\boldsymbol{\gamma}$ can be computed, if a priori knowledge of the sample's thickness is known.

Since $\boldsymbol{\gamma}$, $\boldsymbol{\chi}$, $\boldsymbol{\chi}_{,i}$ and the material properties of the membrane are at hand, Eqs. (14, 15, 18-20) can be used to access the generalized forces ($\mathbf{Q}$, $\mathbf{M}$ and $\mathbf{N}$). Finally, since the displacement $\mathbf{u}$, rotation $\mathbf{a}$ and generalized forces $\mathbf{Q}$, $\mathbf{M}$ and $\mathbf{N}$ are present; and by knowing the frequency in which the membrane is being excited, it is possible to compute and visualize the SI from Eqs. (1-4).

Apart from processing the displacements of a real structure, the validation of the proposed method was also tested on a FE-Method model and is presented in the Appendix of this paper. The SI intensity results that are directly acquired from the model were compared with the energy transmission that is obtained by following the proposed method.

V.   RESULTS

A.   Measurements via the Digital Image Correlation technique

After preparing the set-up described in the Section III and setting the loudspeaker to excite the sample with harmonic excitations ranging from 60 Hz to 170 Hz, the spatial coordinates $\mathbf{x}$ and related global displacements $\mathbf{U}_{exp}^{h/2}$ were processed by the Istra4D software. A total of 24.250 measurement points were correlated for every excitation frequency and a representation of this point cloud can be seen in FIG. 4 (a).

As pointed out, the term $\mathbf{U}_{exp}^{h/2}$ is dependent on the frequency at which the sample was excited. Since the same displacement processing described in Section IV is repeated for every frequency, the intermediate steps towards the SI assessment are displayed next just for the recorded data at 130 Hz. At the end of this section, the computed SI vector fields of that very frequency and others within the mentioned range are also displayed.

B.   Mesh generation & definition of the local coordinate system

Since the DIC system provided the spatial coordinates of the membrane's outer-surface, it is feasible to develop a mesh, whose shape resemble the original surface. As explained in

442 Section IV, quadratic basis functions were used to describe the elements of the mesh, which,

443 in turn, were chosen to be of the triangular type. Since a significant amount of data points

444 were recorded, it was feasible to develop a mesh with elements that were relatively small

445 but would still enclose a significant amount of data points. It was decided to build a mesh

446 whose elements would encompass approximately 12 data points each, a number that would

447 also ensure that the membrane's shape was preserved.

448   A mesh containing 3.964 nodes and 1.906 LST elements was generated, which can be

449 seen in FIG. 2. It can also be noted from the same figure that the mesh was developed only

450 on the regions where the shell theory is applicable, i.e., the free-zones of the sample where

451 no thickness or stiffness heterogeneities are to be found.
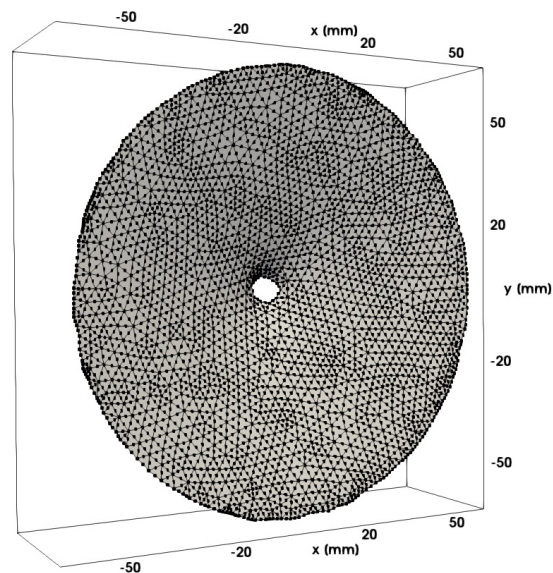
FIG. 2. FE mesh resembling the shape of the circular membrane (1.906 quadratic and flat elements and 3.964 nodes). The points depicted on the figure represent the nodes, where the DoFs are stored.

452 After creating the mesh, one can define the local coordinates, whose directions were used

453 to compute the fields' spatial derivatives. By computing the principal curvature directions

454 of the mesh with the LIBIGL library (Jacobson *et al.*, 2017), the basis vectors $(\mathbf{e}_1, \mathbf{e}_2, \mathbf{e}_3)$

455 were extracted. FIG. 3 presents the tangent local coordinates, which are the guidelines for
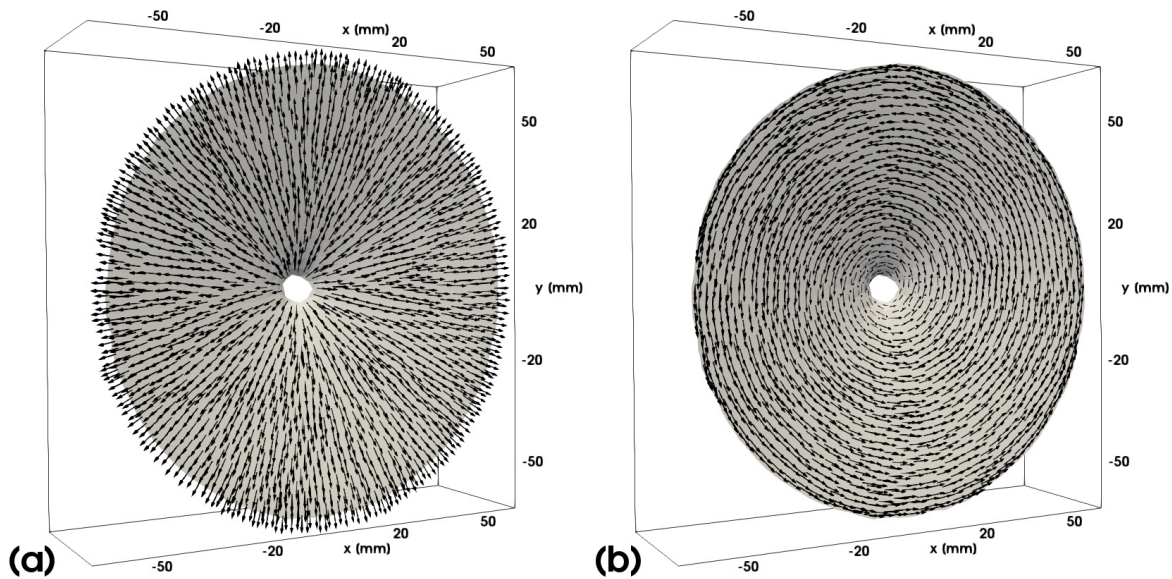
456 the spatial differentiations.

FIG. 3. Representation of the shell's tangent local coordinates $\mathbf{e}_1$ (a) and $\mathbf{e}_2$ (b)

457 Lastly, the quality of the developed mesh was tested on the basis of a shell model, which

458 is shown in the Appendix. From this validation, it was concluded that the developed mesh

459 that follows the Kirchhoff-Love postulates was able to reproduce the SI results of the model.

460 With this validation at hand, the FE mesh was used for further processing.

C.   Computation of global displacements & rotations

462   With the quadratic mesh, the displacement $\mathbf{U}^{h/2}_{exp}$ and related positions $\mathbf{x}$ at hand, Eq. (27)

463   could be used to projected the experimental data on the nodes of the mesh and the global

464   displacement denoted as $\tilde{\mathbf{U}}^{h/2}$ was computed. FIG. 4 displays the magnitude of the global

465   displacement before ($|\mathbf{U}^{h/2}_{exp}|$) and after ($|\tilde{\mathbf{U}}^{h/2}|$) the projection. The three global components

466   of $\tilde{\mathbf{U}}^{h/2}$ are also displayed separately in FIG. 5.
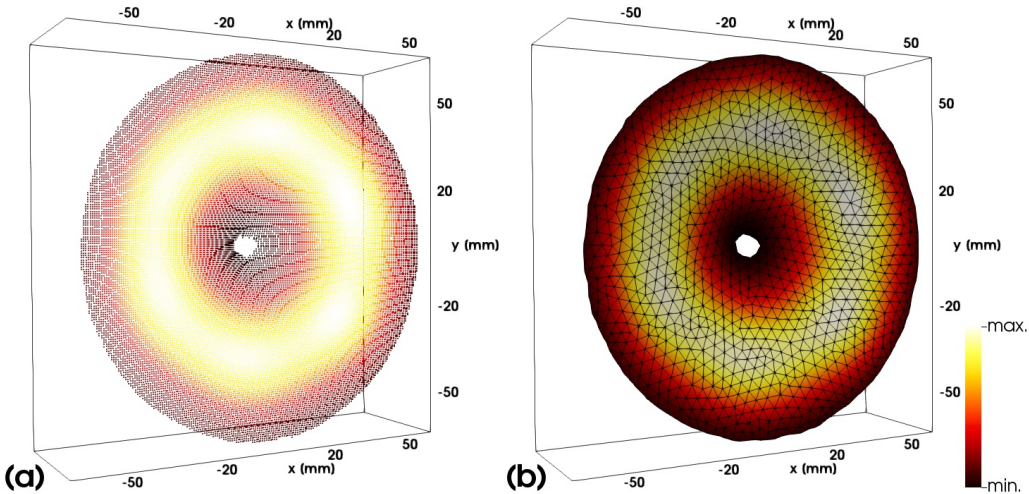
FIG. 4. Projection of data from the dense point cloud to the quadratic mesh. FIG. (a) displays

the term $|\mathbf{U}^{h/2}_{exp}|$ on 24.250 measured points. FIG. (b) displays the projected displacements $|\tilde{\mathbf{U}}^{h/2}|$

on the nodes of the mesh (color online).

467   Since $\tilde{\mathbf{U}}^{h/2}$ has been computed, one can calculate $\mathbf{n}_{def}$ of the mesh under its deformed

468   configuration, so the global rotation $\tilde{\mathbf{A}}$ can be assessed through Eq. (28). The magnitude

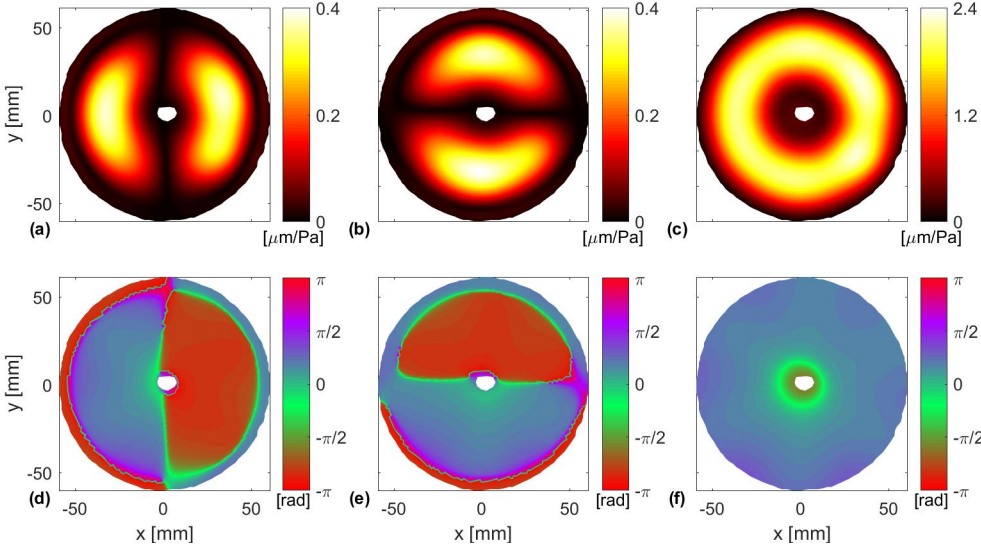469   and relative phase of the components of this term are presented in FIG. 6.

FIG. 5. Components of the global displacement $\tilde{\mathbf{U}}^{h/2}$ in the directions $\mathbf{e}_x$ [(a),(d)], $\mathbf{e}_y$ [(b),(e)] and $\mathbf{e}_z$ [(c),(f)]. The 1st row [(a)-(c)] presents the absolute value of these components, while the 2nd one [(d)-(f)] displays their relative phase with respect to the pressure excitation (color online).
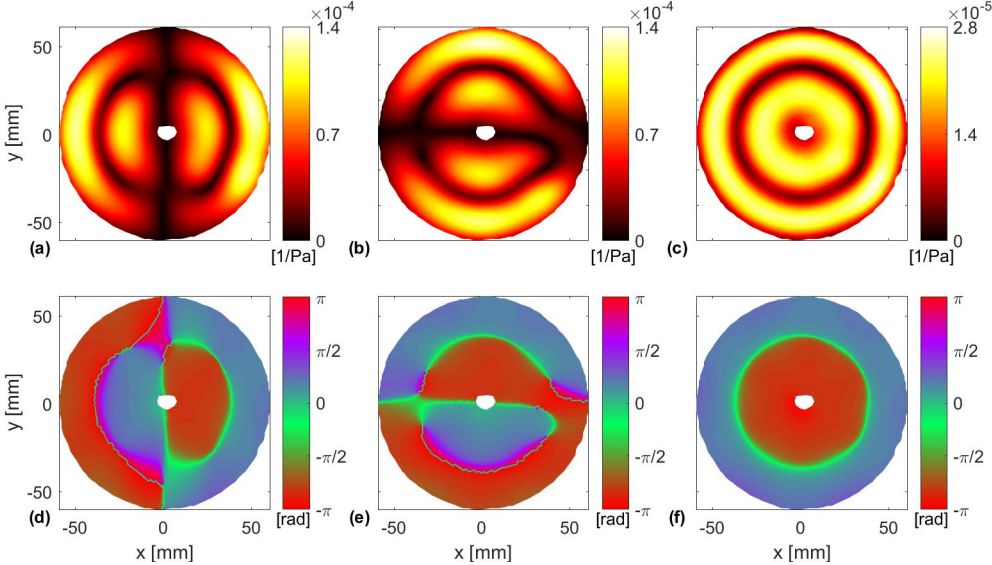

FIG. 6. Components of the global rotation $\tilde{\mathbf{A}}$ in the directions $\mathbf{e}_x$ [(a),(d)], $\mathbf{e}_y$ [(b),(e)] and $\mathbf{e}_z$ [(c),(f)] (color online)

⁴⁷⁰ **D. Data processing**

⁴⁷¹   At this step, the mesh contains 6 global degrees of freedom ($\tilde{\mathbf{U}}^{h/2}$ and $\tilde{\mathbf{A}}$) on each of its

⁴⁷² nodes (shown in FIG. 5 and FIG. 6) and the local coordinates ($\mathbf{e}_1$, $\mathbf{e}_2$, $\mathbf{e}_3$) are also at hand

⁴⁷³ (FIG. 3). By following the description shown in Section II E, the mentioned terms can be

⁴⁷⁴ used to compute the local displacement and rotation, i.e., $\tilde{\mathbf{u}}^{h/2}$ or $\tilde{\mathbf{a}}$.

⁴⁷⁵   The estimation of these terms and their spatial derivatives are then computed at the

⁴⁷⁶ barycentric coordinates of each element Eqs. (30-32). At the end of this process, the terms

⁴⁷⁷ $\mathbf{u}^{h/2}$, $\mathbf{u}^{h/2}_{,i}$ or $\mathbf{a}$, $\mathbf{a}_{,i}$ and $\mathbf{a}_{,ij}$ are available and, in turn, the Green-Lagrange strain at the

⁴⁷⁸ outer-surface $\boldsymbol{\varepsilon}^{h/2}$ [Eqs. (9)], bending curvature $\boldsymbol{\chi}$ [Eqs. (10)] and its first-order derivative

⁴⁷⁹ $\boldsymbol{\chi}_{,i}$ [Eqs. (21)] can also be assessed.

⁴⁸⁰   The last step consists in using the Eqs. (22, 23) to assess the displacement $\mathbf{u}$ and mem-

⁴⁸¹ brane strain $\boldsymbol{\gamma}$ on the shell's mid-surface. All terms from both equations are presented in

⁴⁸² FIG. 7 [terms of Eq. (22)] and FIG. 8 [terms of Eq. (23)] with respect to the local coordinate

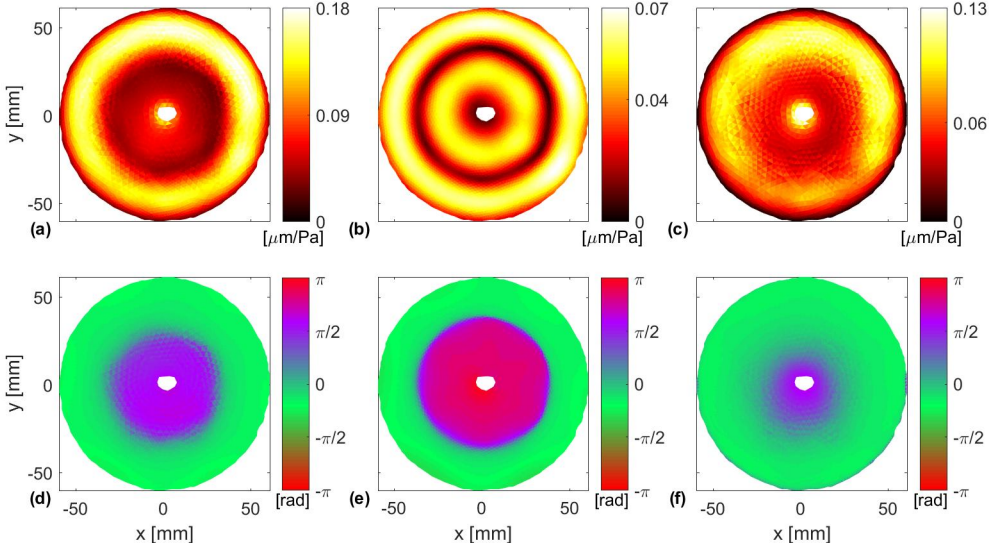⁴⁸³ $\mathbf{e}_1$ as examples.

FIG. 7. Representation of the terms of Eq. (22) from the direction $\mathbf{e}_1$ after data processing. The displayed scalar data are $u_1^{h/2}$ [(a),(d)], $\frac{h}{2}a_1$ [(b),(e)] and u_1 [(c),(f)] (color online).
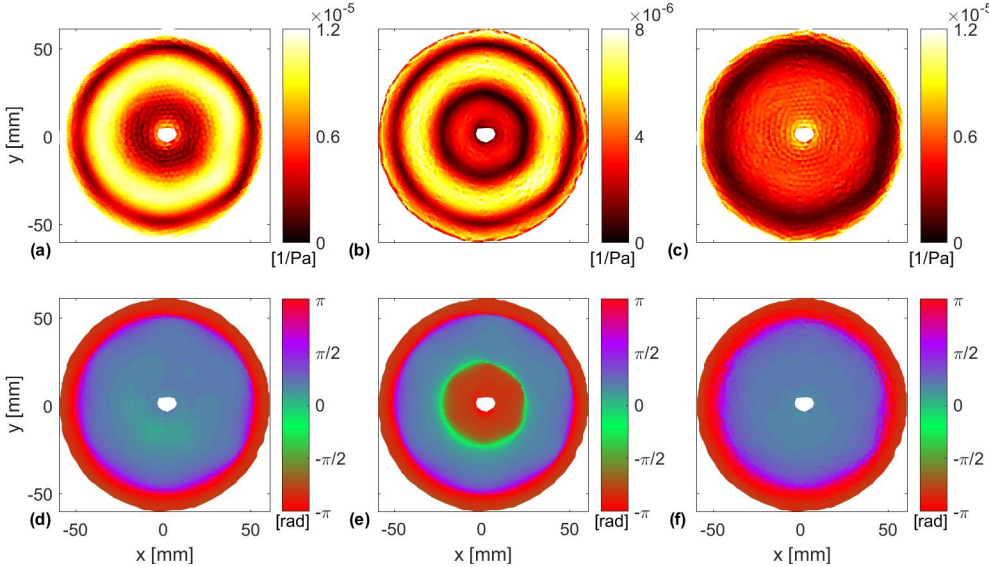

FIG. 8. Representation of the terms of Eq. (23) from the direction $\mathbf{e}_1$ after data processing. The displayed scalar data are $\varepsilon_{11}^{h/2}$ [(a),(d)], $\frac{h}{2}\chi_{11}$ [(b),(e)] and γ_{11} [(c),(f)] (color online).

By having a priori knowledge of the membrane's material properties, the strains and related derivatives ($\boldsymbol{\gamma}$, $\boldsymbol{\chi}$ and $\boldsymbol{\chi}_{,i}$), all terms at the right-hand side of Eqs. (14, 15, 18) are present and the shell's generalized forces ($\mathbf{Q}$, $\mathbf{N}$ and $\mathbf{M}$) are accessible. Moreover, since the terms $\mathbf{u}$ and $\mathbf{a}$ are also available, one has all the necessary components to compute the SI $\mathbf{I}$ from Eqs. (1-4). As examples, the magnitude of the individual SI contributions ($\mathbf{I}_Q$, $\mathbf{I}_M$ and $\mathbf{I}_N$) are presented in FIG. 9.
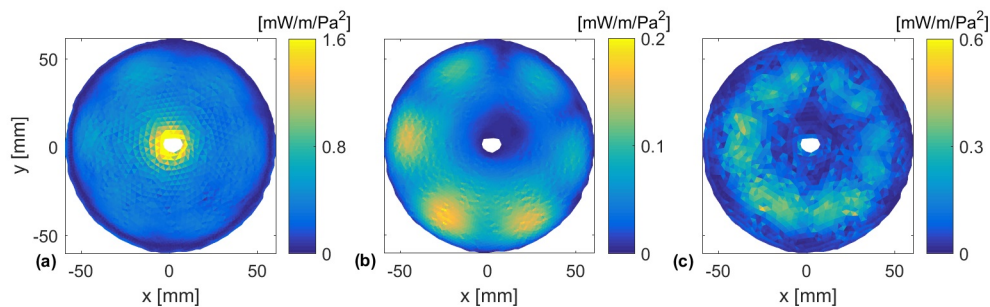

FIG. 9. Individual contributions of the energy transmission taking place on the circular membrane at 130 Hz: The presented data are the normalized values of $|\mathbf{I}_N|$ (a), $|\mathbf{I}_M|$ (b), and $|\mathbf{I}_Q|$ (c) (color online).

The processing of the shape and displacement data described above was repeated for the terms $\mathbf{U}_{exp}^{h/2}$ recorded under all other excitation frequencies. FIG. 10 displays the total SI vector field from displacement data, which were recorded at 60 Hz, 80 Hz, 130 Hz and 170 Hz.
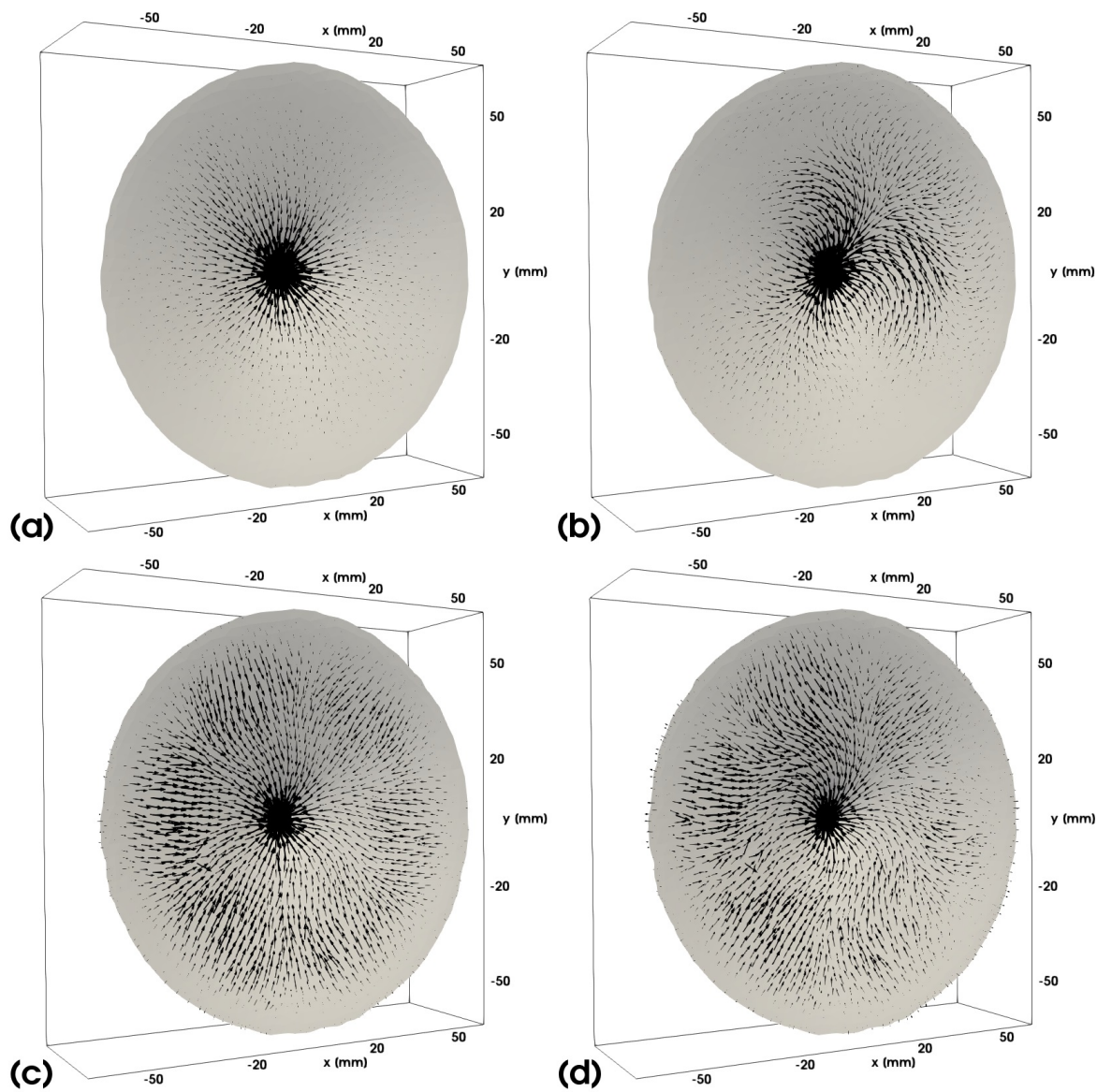
FIG. 10. Structural Intensity vector fields [Eq. (1)] taking place on the circular membrane at 60 Hz (a), 80 Hz (b), 130 Hz (c) and 170 Hz (d)

VI. DISCUSSION & CONCLUSIONS

From FIG. 10, it can be noted that the all SI vector fields contain energy transmission patterns that are qualitatively consistent with the built set-up. It can be noted that a strong vector field convergence occurs on the region were the viscous polymer was installed. Interestingly, it is also worth noting that this convergence takes place through different transmission paths, which shows the strong dependence between the SI results and the excitation frequency.

By analyzing the individual contributions of energy transmission from the generalized forces at 130 Hz (FIG. 9), it could be seen that the component related to the membrane force was not just non-negligible, but it was, by far, the most important term for the energy transmission. The strong relation between the total SI and individual power contribution of the membrane force $\mathbf{N}$ was present in all recorded frequencies and corroborates with the statement that axial waves need to be taken into account when irregular shells are being analyzed (Ventsel and Krauthammer, 2001).

Even though just experimental data from a sample's outer-surface are available, the proposed method could estimate SI results from the sample's mid-surface by invoking assumptions based on the Kirchhoff-Love postulates and approximations regarding the mesh. Moreover and to the authors' knowledge, the only works describing the SI assessement on shells require the principle curvatures of the sample to be alligned with analytical coordinate systems, such as the study on a cylindrical shell presented in (Williams, 1991). This is not the case for the strategy described in this work, which is appicable on shells with arbitrary

shape configurations. Moreover, the data differentiation via FE basis functions was not common in works related to the study of energy flow. The most well-known techniques to compute spatial derivatives are either through the finite difference method (Arruda and Mas, 1998; Schmidt, 2009) or by processing the fields in the wavenumber domain (Arruda, 1992; Lopes *et al.*, 2006; Morikawa *et al.*, 1996; Pascal *et al.*, 1996, 2002, 2006).

The proposed method showed reliable results when the energy transmission paths and their quantitative contributions were compared with the SI presented in a shell model (shown in the Appendix). It is also worth noting that the mentioned model was based on the Mindlin-Reissner theory, while the proposed method is built upon the Kirchhoff-Love plate model. Even though the latter neglects the curvatures and shear strains for the individual elements, the estimated SI converged towards the real numerical solution as it can be noted in FIG. 12 (c,d) and FIG. 13.

By knowing that the proposed approach preserves the information regarding the SI, it can be stated that this procedure is reliable to estimate the strains and the energy transmission on the mid-surface just with the displacements on the outer-surface at hand. Therefore, due to the validation of this work via a shell model and to the results shown in FIG. 9 and FIG. 10, it can be said that the strategy to project experimental data via the FE approximation in combination with data differentiation via quadratic shape functions showed to be a meaningful approach to assess transmission paths of arbitrary shells.

ACKNOWLEDGMENTS

APPENDIX: VALIDITY OF THE STRUCTURAL INTENSITY ASSESSMENT

A shell model that follows the Mindlin-Reissner theory was created in a FE-Method software (COMSOL® Multiphysics 5.2 a, Burlington, Massachusetts, USA) and is represented in FIG. 11. The geometry was generated on the basis of the point cloud **x** shown in FIG. 4 (a).

Since the purpose of this model is to validate the method described in Section IV, it was decided to export the numerical displacement data in such a way that it would resemble the experimental $\mathbf{U}_{exp}^{h/2}$ described in Section V A. To mimic the densely populated measurement points, a refined mesh containing 19.615 nodes was generated over the geometry shown in FIG. 11.

The nodes located at the circumference of this model were clamped, a viscous damper of $1 \, \mathrm{N \cdot s/m}$ was applied at the center of the membrane to simulate the viscous effects of the polymer strip (blue elements shown in FIG. 11) and an uniform and harmonic pressure at 100 Hz was applied on the geometry's free-zones to mimic the harmonic excitation. Lastly, the material properties and thickness of the shell model were set to be the equal to the ones provided in the Section III.

The results provided by the model are shown in the 1st column of FIG. 12. FIG. 12 (a) displays the numerical displacement located at the nodes of the mesh and FIG. 12 (c) shows the related SI vector fields. From here, one can compare the original SI results of FIG. 12 (c) with the energy transmission that can be estimated through the process described in Section IV.

Firstly, the global displacements located at the nodes of this model [FIG. 12 (a)] were exported and Eq. (27) was used to project the global displacement field on the mesh shown in FIG. 2. A representation of this projection can be seen in FIG. 12 (b). By following the data processing shown in Section IV, the total SI could be assessed and visualized [FIG. 12 (d)]. By comparing the energy transmission of the model [FIG. 12 (c)] and the processed SI from the proposed method [FIG. 12 (d)], it can be noticed that both vector fields have similiar paths over the geometry's domain.

The SI contributions of the membrane forces $\mathbf{I}_N$, bending moments $\mathbf{I}_M$ and shear forces $\mathbf{I}_Q$ of the model can also be analyzed separately. The 1$^{\text{st}}$ row of FIG. 13 displays the absolute value of these vector fields. The 2$^{\text{nd}}$ row of the same figure displays these very values from the SI shown in FIG. 12 (d), i.e., the energy flow computed via the proposed method.

By comparing the fields that were directly computed from the COMSOL model [FIG. 13 (a-c)] with the ones calculated on the basis of the Kirchhoff-Love plate model [FIG. 13 (d-f)], it can be noted that they are quantitatively consistent with each other. Due to this comparison, it can be stated that the proposed method not just computes the energy paths taking place on a shell [FIG. 12 (d)], but also preserves the SI magnitudes [FIG. 13 (d-f)], despite the stronger assumptions being imposed on the Kirchhoff-Love plate model.
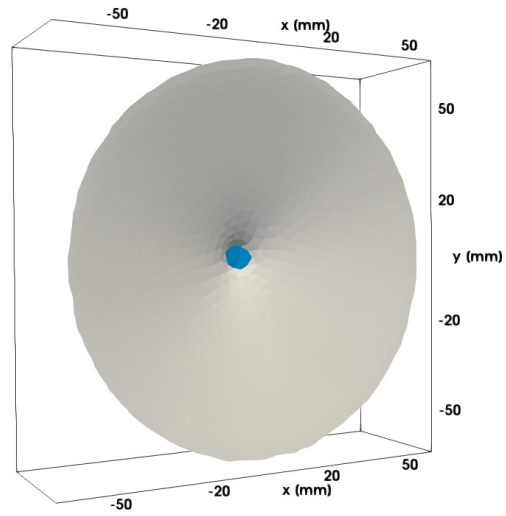
FIG. 11. Representation of the model's geometry developed for validation (color online)
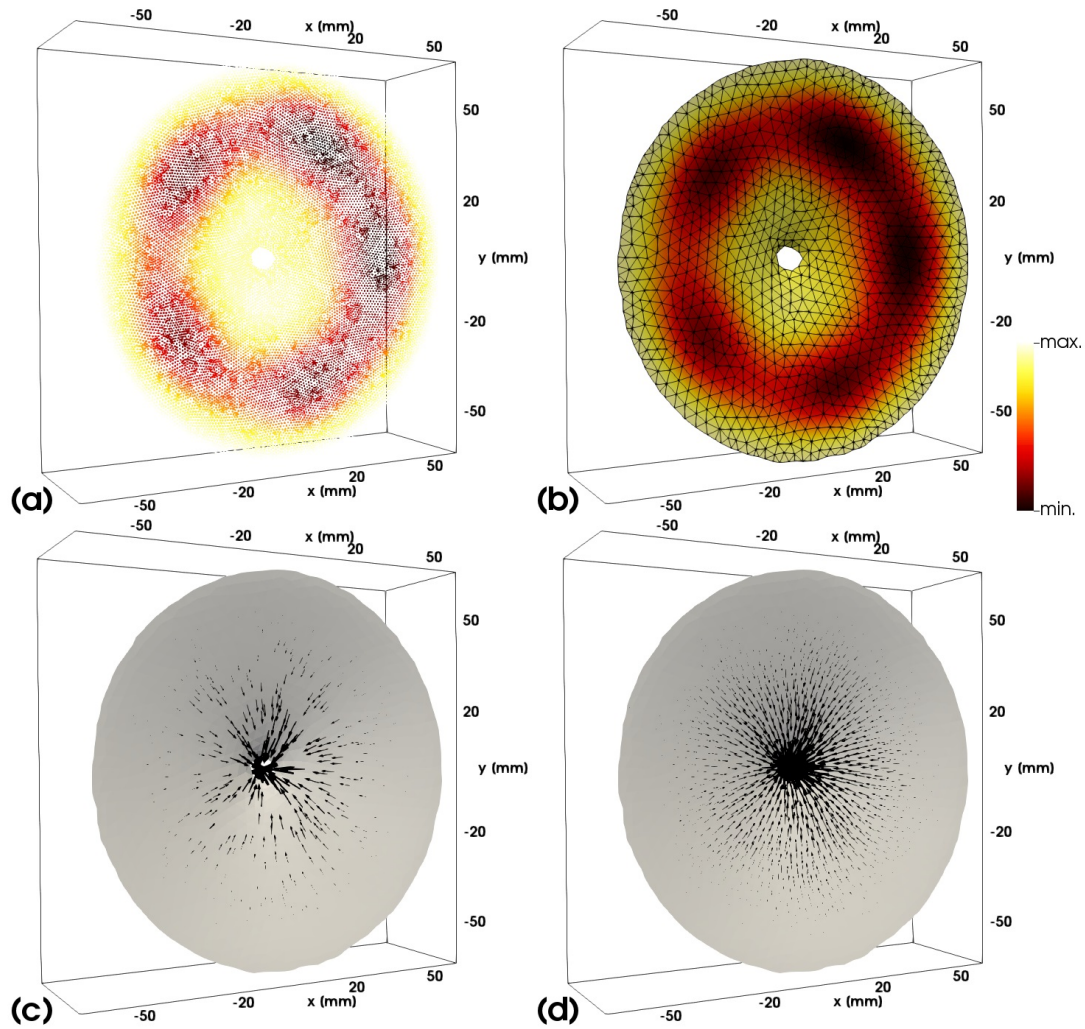
FIG. 12. Representation of displacement data [(a)-(b)] and SI [(c)-(d)]. The terms displayed on the 1st column [(a),(c)] were obtained from the FE software and are directly acquirable after the simulation's conclusion. The 2nd column [(b),(d)] displays the same terms that can be visualized on the basis of the method presented in Section IV (color online).
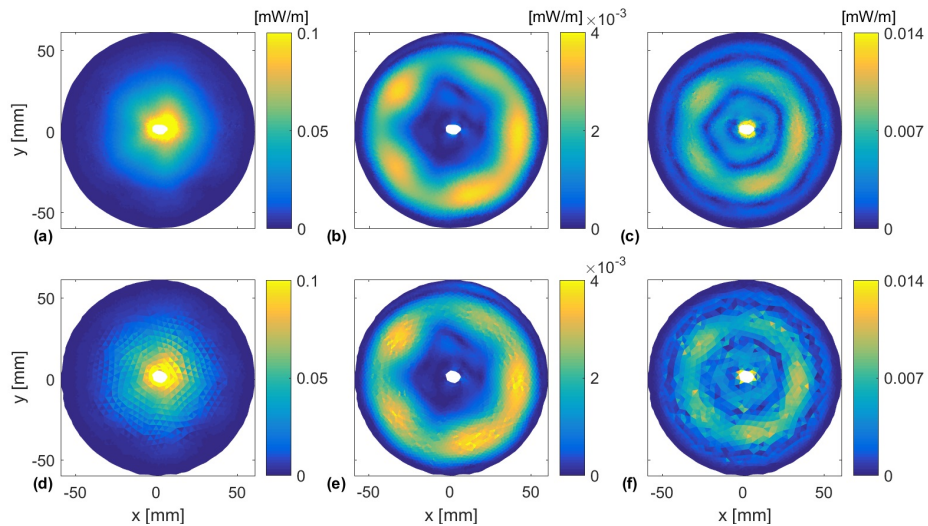
FIG. 13. Individual contributions of the energy transmission taking place on the model: The presented data are values of $|\mathbf{I}_N|$ (a,d), $|\mathbf{I}_M|$ (b,e), and $|\mathbf{I}_Q|$ (c,f). The 1$^{\text{st}}$ row displays these fields that were computed via the COMSOL model. The 2$^{\text{nd}}$ row shows the SI contributions, which were processed via the proposed mehtod (color online).

575

Al Ba'ba'a, H. B., Attarzadeh, M. A., and Nouh, M. (**2018**). "Experimental evaluation of structural intensity in 2d plate-type locally resonant elastic metamaterials," Journal of Applied Mechanics .

Al Ba'ba'a, H. B., and Nouh, M. (**2017**). "Mechanics of longitudinal and flexural locally resonant elastic metamaterials using a structural power flow approach," International Journal of Mechanical Sciences **122**, 341–354.

Arruda, J., and Mas, P. (**1998**). "Localizing energy sources and sinks in plates using power flow maps computed from laser vibrometer measurements," Shock and Vibration **5**(4), 235–253.

Arruda, J. F. (**1992**). "Surface smoothing and partial spatial derivatives computation using a regressive discrete fourier series," Mechanical Systems and Signal Processing **6**(1), 41–50.

Avril, S., Feissel, P., Pierron, F., and Villon, P. (**2009**). "Comparison of two approaches for differentiating full-field data in solid mechanics," Measurement Science and Technology **21**(1), 015703.

Avril, S., and Pierron, F. (**2007**). "General framework for the identification of constitutive parameters from full-field measurements in linear elasticity," International Journal of Solids and Structures **44**(14-15), 4978–5002.

Bischoff, M., and Ramm, E. (**1997**). "Shear deformable shell elements for large strains and rotations," International Journal for Numerical Methods in Engineering **40**(23), 4427–4449.

Büchter, N., Ramm, E., and Roehl, D. (**1994**). "Three-dimensional extension of non-linear shell formulation based on the enhanced assumed strain concept," International journal

for numerical methods in engineering **37**(15), 2551–2568.

Chapelle, D., and Bathe, K.-J. (**2010**). *The finite element analysis of shells-fundamentals* (Springer Science & Business Media).

Cho, D.-S., Choi, T.-M., Kim, J.-H., and Vladimir, N. (**2016**). "Structural intensity analysis of stepped thickness rectangular plates utilizing the finite element method," Thin-walled structures **109**, 1–12.

Cho, D.-S., Choi, T.-M., Kim, J.-H., and Vladimir, N. (**2017**). "Dominant components of vibrational energy flow in stiffened panels analysed by the structural intensity technique," International Journal of Naval Architecture and Ocean Engineering .

Cho, D.-S., Kim, K.-S., and Kim, B.-H. (**2010**). "Structural intensity analysis of a large container carrier under harmonic excitations of propulsion system," International Journal of Naval Architecture and Ocean Engineering **2**(2), 87–95.

Dhatt, G., Marcotte, L., and Matte, Y. (**1986**). "A new triangular discrete kirchhoff plate/shell element," International journal for numerical methods in engineering **23**(3), 453–470.

Eck, T., and Walsh, S. J. (**2012**). "Measurement of vibrational energy flow in a plate with high energy flow boundary crossing using electronic speckle pattern interferometry," Applied Acoustics **73**(9), 936–951.

Feng, Z., and Rowlands, R. (**1991**). "Smoothing finite-element and experimental hybrid technique for stress analyzing composites," Computers & Structures **39**(6), 631–639.

Gavrić, L., and Pavić, G. (**1993**). "A finite element method for computation of structural intensity by the normal mode approach," Journal of sound and vibration **164**(1), 29–43.

Hambric, S. A. (**1990**). "Power flow and mechanical intensity calculations in structural finite element analysis," Journal of Vibration and Acoustics **112**(4), 542–549.

Hambric, S. A., and Szwerc, R. P. (**1999**). "Predictions of structural intensity fields using solid finite elements," Noise Control Engineering Journal **47**(6), 209–217.

Jacobson, A., Panozzo, D. *et al.* (**2017**). "libigl: A simple C++ geometry processing library" http://libigl.github.io/libigl/ (Last viewed 1/6/2018).

Kraus, H. (**1967**). *Thin elastic shells* (John Wiley & Sons).

Lamberti, A., and Semperlotti, F. (**2013**). "Detecting closing delaminations in laminated composite plates using nonlinear structural intensity and time reversal mirrors," Smart Materials and Structures **22**(12), 125006.

Lee, H., Lim, S., and Khun, M. (**2006**). "Diversion of energy flow near crack tips of a vibrating plate using the structural intensity technique," Journal of Sound and Vibration **296**(3), 602–622.

Li, Y., and Lai, J. (**2000**). "Prediction of surface mobility of a finite plate with uniform force excitation by structural intensity," Applied Acoustics **60**(3), 371–383.

Liu, Z., Lee, H., and Lu, C. (**2005**). "Structural intensity study of plates under low-velocity impact," International Journal of Impact Engineering **31**(8), 957–975.

Lopes, H., Guedes, R. M., and Vaz, M. (**2006**). "Techniques in numerical differentiation of experimentally noisy data," in *Proceedings of the 5th International Conference of Mechanical & Materials in Design*, July 24-26, Porto, Portugal, pp. 27–28.

Miguel, C. J., and Feit, D. (**1986**). *Sound, structures, and their interaction* (Cambridge, MA: MIT Press).

641 Morikawa, R., Ueha, S., and Nakamura, K. (**1996**). "Error evaluation of the structural in-

642 tensity measured with a scanning laser doppler vibrometer and ak-space signal processing,"

643 The Journal of the Acoustical Society of America **99**(5), 2913–2921.

644 Morse, P. M., and Feshbach, H. (**1946**). *Methods of theoretical physics* (Technology Press,

645 New York).

646 Murthy, S., and Gallagher, R. (**1986**). "A triangular thin-shell finite element based on

647 discrete kirchhoff theory," Computer methods in applied mechanics and engineering **54**(2),

648 197–222.

649 Noiseux, D. (**1970**). "Measurement of power flow in uniform beams and plates," The Journal

650 of the Acoustical Society of America **47**(1B), 238–247.

651 Novozhilov, V. V. (**1959**). *Thin shell theory* (P. Noordhoff).

652 Panozzo, D., Puppo, E., and Rocca, L. (**2010**). "Efficient multi-scale curvature and crease

653 estimation," in *Proceedings of the 2nd International Workshop on Computer Graphics,*

654 *Computer Vision and Mathematics*, GraVisMa 2010, September 7-10, Brno, Czech Re-

655 public.

656 Pascal, J., Loyau, T., and Mann III, J. (**1990**). "Structural intensity from spatial fourier

657 transformation and bahim acoustical holography method," Proc. Cong. On Structural

658 Intensity and Vibrational Energy Flow 197–204.

659 Pascal, J.-C., Carniel, X., Chalvidan, V., and Smigielski, P. (**1996**). "Determination of phase

660 and magnitude of vibration for energy flow measurements in a plate using holographic

661 interferometry," Optics and Lasers in Engineering **25**(4-5), 343–360.

Pascal, J.-C., Li, J.-F., and Carniel, X. (**2002**). "Wavenumber processing techniques to determine structural intensity and its divergence from optical measurements without leakage effects," Shock and vibration **9**(1, 2), 57–66.

Pascal, J.-C., Carniel, X., and Li, J.-F. (**2006**). "Characterisation of a dissipative assembly using structural intensity measurements and energy conservation equation," Mechanical systems and signal processing **20**(6), 1300–1311.

Pavić, G. (**1976**). "Measurement of structure borne wave intensity, part i: Formulation of the methods," Journal of Sound and Vibration **49**(2), 221–230.

Petrone, G., De Vendittis, M., De Rosa, S., and Franco, F. (**2016**). "Numerical and experimental investigations on structural intensity in plates," Composite Structures **140**, 94–105.

Pires, F., Muyshondt, P., Keustermans, W., Vanlanduit, S., Roozen, N., and Dirckx, J. (**2018**). "Structural intensity analysis of flat plates based on digital stroboscopic holography measurements," Journal of Sound and Vibration **428**, 168–178.

Romano, A., Williams, E., Russo, K., and Schuette, L. (**1992**). "On the visualization and analysis of fluid-structure interaction from the perspective of instantaneous intensity," Le Journal de Physique IV **2**(C1), C1–597.

Romano, A. J., Abraham, P. B., and Williams, E. G. (**1990**). "A poynting vector formulation for thin shells and plates, and its application to structural intensity analysis and source localization. part i: Theory," The Journal of the Acoustical Society of America **87**(3), 1166–1175.

Roozen, N., Guyader, J., and Glorieux, C. (**2015**). "Measurement-based determination of the irrotational part of the structural intensity by means of test functional series expansion," Journal of Sound and Vibration **356**, 168–180.

Saijyou, K. (**2007**). "Measurement of structural intensity using boundary element method-based nearfield acoustical holography," The Journal of the Acoustical Society of America **121**(6), 3493–3500.

Schaal, C., Ebert, J., Bös, J., and Melz, T. (**2016**). "Relation between structural intensity-based scalars and sound radiation using the example of plate-rib models," Journal of Vibration and Acoustics **138**(4), 041011.

Schmidt, W. T. (**2009**). "Open-crack damage assessments of aluminum panels using structural intensity-based techniques," Ph.D. thesis, The Pennsylvania State University, State College, PA.

Schreier, H., Orteu, J.-J., and Sutton, M. A. (**2009**). *Image correlation for shape, motion and deformation measurements* (Springer US).

Semperlotti, F., and Conlon, S. C. (**2010**). "Structural damage identification in plates via nonlinear structural intensity maps," The Journal of the Acoustical Society of America **127**(2), EL48–EL53.

Shepherd, M. R., Conlon, S. C., Semperlotti, F., and Hambric, S. A. (**2012**). "Structural intensity modeling and simulations for damage detection," Journal of Vibration and Acoustics **134**(5), 051004.

Tian, X., Liu, G., Gao, Z., Chen, P., and Mu, W. (**2017**). "Crack detection in offshore platform structure based on structural intensity approach," Journal of Sound and Vibration

705 **389**, 236–249.

706 Tran, T., Lee, H., and Lim, S. (**2007**). "Structural intensity analysis of thin laminated

707 composite plates subjected to thermally induced vibration," Composite structures **78**(1),

708 70–83.

709 Ventsel, E., and Krauthammer, T. (**2001**). *Thin plates and shells: theory: analysis, and*

710 *applications* (CRC press).

711 Vuye, C. (**2011**). "Measurement and modeling of sound and vibration fields using a scanning

712 laser doppler vibrometer," Ph.D. thesis.

713 Wagner, W., and Gruttmann, F. (**1994**). "A simple finite rotation formulation for composite

714 shell elements," Engineering Computations **11**(2), 145–176.

715 Williams, E. G. (**1991**). "Structural intensity in thin cylindrical shells," The Journal of the

716 Acoustical Society of America **89**(4), 1615–1622.

717 Xu, X., Lee, H., and Lu, C. (**2004**a). "Numerical study on energy transmission for rotating

718 hard disk systems by structural intensity technique," International journal of mechanical

719 sciences **46**(4), 639–652.

720 Xu, X., Lee, H., and Lu, C. (**2004**b). "The structural intensities of composite plates with a

721 hole," Composite Structures **65**(3-4), 493–498.

722 Xu, X., Lee, H., and Lu, C. (**2005**). "Power flow paths in stiffened plates," Journal of Sound

723 and Vibration **282**(3-5), 1264–1272.

724 Zhang, Y. (**1993**). "An experimental method for structural intensity and source location,"

725 Ph.D. thesis.

726 Zhang, Y., and Mann III, J. A. (**1996**). "Examples of using structural intensity and the force

727 distribution to study vibrating plates," The Journal of the Acoustical Society of America

728 **99**(1), 354–361.

729 Zienkiewicz, O. C., Taylor, R. L., Zienkiewicz, O. C., and Taylor, R. L. (**1977**). *The finite*

730 *element method*, **3** (McGraw-hill London).